PAPER

CoFe$_2$O$_4$ nanoparticles decorated MoS$_2$-reduced graphene oxide nanocomposite for improved microwave absorption and shielding performance

Jagdees Prasad,[a] Ashwani Kumar Singh, [iD][a] Krishna Kamal Haldar,[b]
Monika Tomar, [iD][b] Vinay Gupta[b] and Kedar Singh [iD]*[a]

Magnetic CoFe$_2$O$_4$ nanoparticles decorated onto the surface of a MoS$_2$-reduced graphene oxide (MoS$_2$-rGO/CoFe$_2$O$_4$) nanocomposite were synthesized by a simple two-step hydrothermal method. The electromagnetic (EM) wave absorption performance and electromagnetic interference (EMI) shielding effectiveness of the materials were examined in the frequency range of 8.0–12.0 GHz (X-band). The MoS$_2$-rGO/CoFe$_2$O$_4$ nanocomposite was characterized by various tools such as X-ray diffraction, Raman spectroscopy, scanning electron microscopy, and transmission electron microscopy. High-resolution transmission electron microscopy results confirmed the decoration of magnetic nanoparticles onto the surface of the MoS$_2$-rGO nanocomposite with a diameter of 8–12 nm. The multiple interfacial polarization, moderate impedance matching, and defect dipole polarization improve the dielectric and magnetic loss of the materials, which leads to strong attenuation loss ability of incident EM energy within the shield. The pure MoS$_2$-rGO nanocomposite represents total shielding effectiveness (SE$_T$ ~16.52 dB), while the MoS$_2$-rGO/CoFe$_2$O$_4$ nanocomposite exhibits total shielding effectiveness (SE$_T$ ~19.26 dB) over the entire frequency range. It may be explained that the magnetic nanoparticles (CoFe$_2$O$_4$) serve as excellent conductive and magnetic fillers with a large surface area, leading to the migration of charge carriers at multi-interfaces.

1. Introduction

In the modern era, the rapid development of telecommunication systems, industrial equipment, and a large number of electronic devices such as cellular phones, loudspeakers, iPads, televisions, radios, laptops, wireless wide area networks (WAN), *etc.* is a significant cause of electromagnetic interference (EMI) pollution in our daily life.[1–5] These devices play an essential role in our daily life and make our life more comfortable; however, the electromagnetic (EM) radiation pollution that they emit within microwave range creates serious EM environmental pollution. EM pollution is increasing globally over time, and not only influences communication systems, electronic equipment, and military weapons, but also causes adverse effects on the health of humans.[6–8] Therefore, in the past few years, considerable effort has been devoted to designing and fabricating ideal high-performance microwave absorption (MA) and EMI shielding materials, which significantly mitigate the increasing problem of serious EMI.[7,9] An ideal EM wave absorbing and shielding material can be widely used in electronic device protection, environmental pollution cleaning, wireless telecommunication, and in human health care, for example. These materials exhibit many essential properties, such as a low density, light weight, thinness, high electrical conductivity, large surface area, wide absorption efficiency range, and good thermal and chemical stability.[10–15] However, superior MA shielding materials should exhibit a good impedance matching condition, in which the relative permittivity (ε_r), and permeability (μ_r) of the material are of the same magnitude.[16,17] According to the classical EM theory, the MA properties of materials are largely affected by dielectric and magnetic losses.[18] All materials with high dielectric or magnetic loss properties only exhibit impedance mismatching, and maximum incident microwaves are strongly reflected instead of absorbed. The shielding properties of these materials primarily depend on reflection, not the absorption coefficient.[19] Hence, excellent MA shielding materials can absorb unwanted EM energy by converting it into thermal energy or other types of energy.[20]

Recently, some highly conductive carbon-based materials such as carbon black, carbon nanotubes, carbon fibers, and graphene, for example, have attracted considerable attention and interest in terms of EM absorption and shielding performance.[21] Isolation of graphene, a single layer of graphite, provides a new platform that may be used as excellent building block materials. Graphene shows a high specific surface area with abundant functional groups and structural defects on its

[a]*School of Physical Sciences, Jawaharlal Nehru University, New Delhi-110067, India. E-mail: kedar@mail.jnu.ac.in*

[b]*Departments of Physics and Astrophysics, Delhi University, New Delhi-110007, India*

surface, leading to multi-interfacial polarization and defect dipole polarization. It has many interesting physical, chemical, and mechanical properties, and is widely used in energy storage devices, light-emitting devices, hydrogen evolution, and in energy conversion due to its high electrical conductivity, thinness, low mass density, light weight, high dielectric loss and easy binding ability with other materials.[22–26] Further, reduced graphene oxide (rGO) exhibits excellent dielectric properties and higher electrical conductivity, but is not considered to have good attenuation loss ability of EM energy due to its impedance mismatching. rGO is a non-magnetic material that leads to relative complex permittivity, and permeability is entirely out of phase.[19] Therefore, introducing $CoFe_2O_4$ nanoparticles onto the surface of an MoS_2-rGO nanocomposite can improve magnetic permeability and magnetic loss in the GHz frequency range. Magnetic nanoparticles can moderate its impedance matching characteristics and strong attenuation loss ability of EM energy with shield materials, and create superb EM wave absorbing and EMI shielding materials.[27]

A layered semiconductor MoS_2 with a hexagonal structure represents a new type of two-dimensional (2D) graphene-like structure consisting of a strong covalently bound S–Mo–S triple layer. Weak van der Waals forces act between vertically stacked MoS_2 nanosheets.[28] This material has recently attracted considerable attention due to its remarkable and desirable physical, chemical, and mechanical properties. MoS_2 has potential applications in diverse areas such as supercapacitors electrodes, high-performance sensors, energy conversion, light-emitting devices, and in hydrogen evolution.[29] MoS_2 also exhibits excellent dielectric loss and possesses a thin and high specific surface area that could successfully increase the propagation path of EM waves inside the sample. It also exhibits many surface defects, including Mo and S vacancies, due to the violent exfoliation process, and works as dipoles under an EM field.[23,30] MoS_2 forms a multiple interface structure and dipole polarization charges on the surface of the nanosheet to enhance the interface polarization and defect dipole polarization for greater attenuation of EM waves.[29] Conjugating MoS_2 with rGO can effectively increase the electrical conductivity due to the close contact between MoS_2 and rGO, and this stable junction is beneficial for charge carrier mobility. A MoS_2-rGO nanocomposite could provide more interfaces and favorable polarization centers for a greater attenuation loss of incident EM energy inside the shield compared with single MoS_2 or rGO nanosheet. Magnetic $CoFe_2O_4$ nanoparticles exhibit excellent properties such as good mechanical and chemical stability, high permeability, a moderate saturation magnetization, high coercivity, and mostly used commercial ferrites.[31] Due to its high magnetic hysteresis loss, eddy current loss, magnetic resonance loss, and effective anisotropy energy, the material exhibits an excellent MA and shielding performance.

In this work, we synthesized an MoS_2-rGO/$CoFe_2O_4$ nanocomposite by a simple two-step hydrothermal technique to improve its dielectric loss and magnetic loss. The phase structure, microstructure, dielectric and magnetic properties of the as-prepared MoS_2-rGO/$CoFe_2O_4$ nanocomposite were characterized by X-ray diffraction (XRD), field-emission scanning

electron microscopy (FESEM), high-resolution transmission electron microscopy (HRTEM), and Vector Network Analyzer, respectively. Decoration of $CoFe_2O_4$ nanoparticles onto the surface of the MoS_2-rGO nanosheet significantly enhanced MA and shielding effectiveness due to moderate impedance matching of materials.

2. Experimental

2.1 Materials and reagents

Ammonium molybdate tetrahydrate, thiourea, ethanol, cobalt(III) acetylacetonate, iron(III) acetylacetonate, oleylamine, and pure graphite powder (99.99%) were purchased from Sigma Aldrich. HNO_3, H_2SO_4, and $KClO_3$ were procured from Fisher Scientific. All chemicals were reagent grade and were used as received without further purification. High purity deionized (DI) water was used in this work as a solvent and for purification.

2.2 Preparation of $CoFe_2O_4$ nanoparticles

$CoFe_2O_4$ nanoparticles were prepared using a facile one-step solvothermal process. In a typical experiment, 0.9 mmol of iron(III) acetylacetonate and 0.45 mmol of cobalt(III) acetylacetonate were mixed and dissolved in 32 ml oleylamine under continuous magnetic stirring for 1 h at ambient temperature to yield a uniform mixture. The reddish uniform solutions were transferred into a 100 ml Teflon-lined stainless-steel autoclave, kept in an oven and maintained at 200 °C for 24 h. After complete reaction, the autoclave was allowed to cool naturally to room temperature, and the final product was collected by centrifuge at 5000 rpm for 10 min. Again, the product was washed several times with ethanol, and finally re-dispersed in 5 ml ethanol for further experimentation.

2.3 Preparation of MoS_2-rGO/$CoFe_2O_4$ nanocomposite

Graphite oxide sheets (GOS) were successfully synthesized from natural bulk graphite powder by a slightly modified Staudenmaier's method.[32] The MoS_2-rGO/$CoFe_2O_4$ nanocomposite was synthesized as follows: first, GOS (4 mg ml^{-1}) were dissolved into 35 ml of DI water by sonication over 1.5 h to form a mixture. Second, 1 mmol of ammonium molybdate tetrahydrate, 30 mmol of thiourea, and a 5 ml solution of $CoFe_2O_4$ nanoparticles in ethanol were dissolved in the above mixture under constant magnetic stirring for 50 min at ambient temperature. Finally, the uniform solution was poured into a Teflon-lined autoclave, kept in an oven and maintained at 220 °C for 24 h. At the end of the reaction, the autoclave was allowed to cool naturally to room temperature, before the black product was collected and cleaned several times with DI water and ethanol, and then dried in a vacuum oven at 60 °C for 10 h. We also synthesized an MoS_2-rGO nanocomposite by the same experiment without introducing $CoFe_2O_4$ nanoparticles, as shown in Fig. 1.

2.4 Characterization tools

The synthesized nanocomposite was characterized by powder XRD (pXRD) measurements from 10° to 80° in 2θ angles with
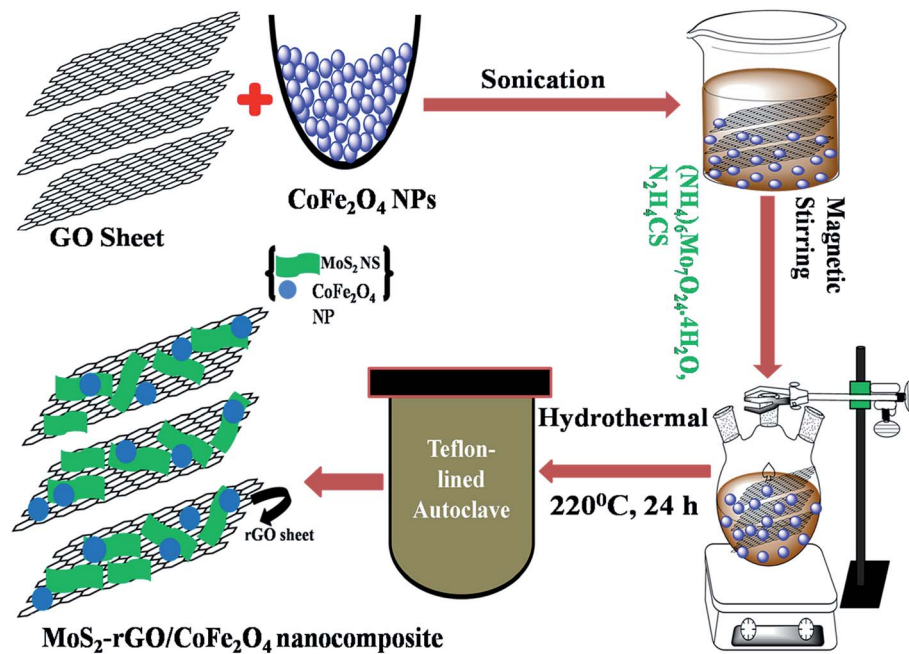
Fig. 1 Schematic illustration of the synthetic route to MoS$_2$-rGO and the MoS$_2$-rGO/CoFe$_2$O$_4$ nanocomposite.

the help of a Rigaku Miniflex-600 diffractometer using Cu-Kα radiation ($\lambda = 1.54056$ Å) operating at 45 kV and a step size of 0.02°. Raman spectra were recorded using a Wi-Tech alpha Germany 300 RA spectrometer system under an argon laser (wavelength $\lambda = 536$ nm) with an output power 20–50 mW. The microstructure, surface morphology and elemental composition of the as-prepared nanocomposite were performed by transmission electron microscope (TEM; model JEOL JEM-2100F) operating at an accelerating voltage of 200 kV, and scanning electron microscope (SEM; Zeiss EVO40) operating at 20 kV to investigate the morphology of the sample. The EM wave absorption parameter and shielding effectiveness measurements were performed using a two-port Vector Network Analyzer (Agilent E8362B) to calculate absorption properties in the frequency range of 8–12 GHz. The powder samples were prepared by pressing into thick rectangular shaped pellets using a hydraulic press at 6 ton pressure. The rectangular shaped sample was inserted into two copper sample holders and sandwiched between two waveguides.

3. Results and discussion

3.1 Phase composition and Raman spectra

The phase formation and crystal structure of CoFe$_2$O$_4$ (a), MoS$_2$-rGO (b), and MoS$_2$-rGO/CoFe$_2$O$_4$ (c) nanocomposites were investigated using pXRD, as depicted in Fig. 2. In Fig. 2a, diffraction peaks located at $2\theta = 18.22°$, 30.18°, 35.44°, 42.96°, 53.36°, 56.74°, 62.50°, and 74.04°, indexed as (111), (220), (311), (400), (422), (511), (440), and (533) crystal planes of pure CoFe$_2$O$_4$ nanoparticles, respectively.[33] The XRD pattern of pure MoS$_2$-rGO nanocomposite exhibits four diffraction peaks at around $2\theta = 14.02°$, 33.56°, 39.82°, and 58.50° are well assigned

to the (002), (100), (103), and (110) lattice planes of a hexagonal MoS$_2$ crystal structure, as depicted in Fig. 2b.[34–38] As shown in Fig. 2c, the lattice planes of CoFe$_2$O$_4$ nanoparticles did not change after hybridization with MoS$_2$-rGO, and are present in the MoS$_2$-rGO/CoFe$_2$O$_4$ nanocomposite. However, the intensity of CoFe$_2$O$_4$ nanoparticles in the hybrid nanocomposite appears weaker than in pure CoFe$_2$O$_4$ nanoparticles. The reason appears to be the small amount of CoFe$_2$O$_4$ nanoparticles in the MoS$_2$-rGO nanocomposite. Low crystallinity and a broad diffraction peak (002) for rGO (Fig. 2c) appeared at around $2\theta = 26.16°$, which may be ascribed to the weak scattering power and low concentration of rGO in the hybrid nanocomposite; however, the signature of rGO was readily identified by Raman spectroscopy, as shown in Fig. 3.[39] No other additional diffraction peaks are observed, suggesting the successful formation of a 3D flower-like MoS$_2$-rGO/CoFe$_2$O$_4$ nanocomposite during the hydrothermal process.

Raman spectroscopy was used to observe crystal structure changes of carbon atoms in MoS$_2$-rGO (a) and MoS$_2$-rGO/CoFe$_2$O$_4$ (b) nanocomposite, as shown in Fig. 3. In Fig. 3a, two characteristic peaks of hexagonal MoS$_2$ are displayed at 386.06 cm^{-1} and 408.82 cm^{-1}, respectively, in the MoS$_2$-rGO nanocomposite, belonging to lower energy E$^1_{2g}$ (in-plane Mo–S phonon mode) and higher energy A$_{1g}$ (out of plane vibration of S atom) Raman modes.[40] There are two distinct strong peaks of rGO positioned at 1358 cm^{-1} (random arrangement of graphite crystallites) called the D-band, and at 1586 cm^{-1} (stretching vibration of C atoms in the sp^2 hybridized plane) called the G-band, as illustrated in Fig. 3c and d.[41] It is clear that the intensity ratio of the D- and G-band (I_D/I_G) for MoS$_2$-rGO was observed at 0.9927, and gradually increased as CoFe$_2$O$_4$ nanoparticles were introduced and were found at 1.0021 for the
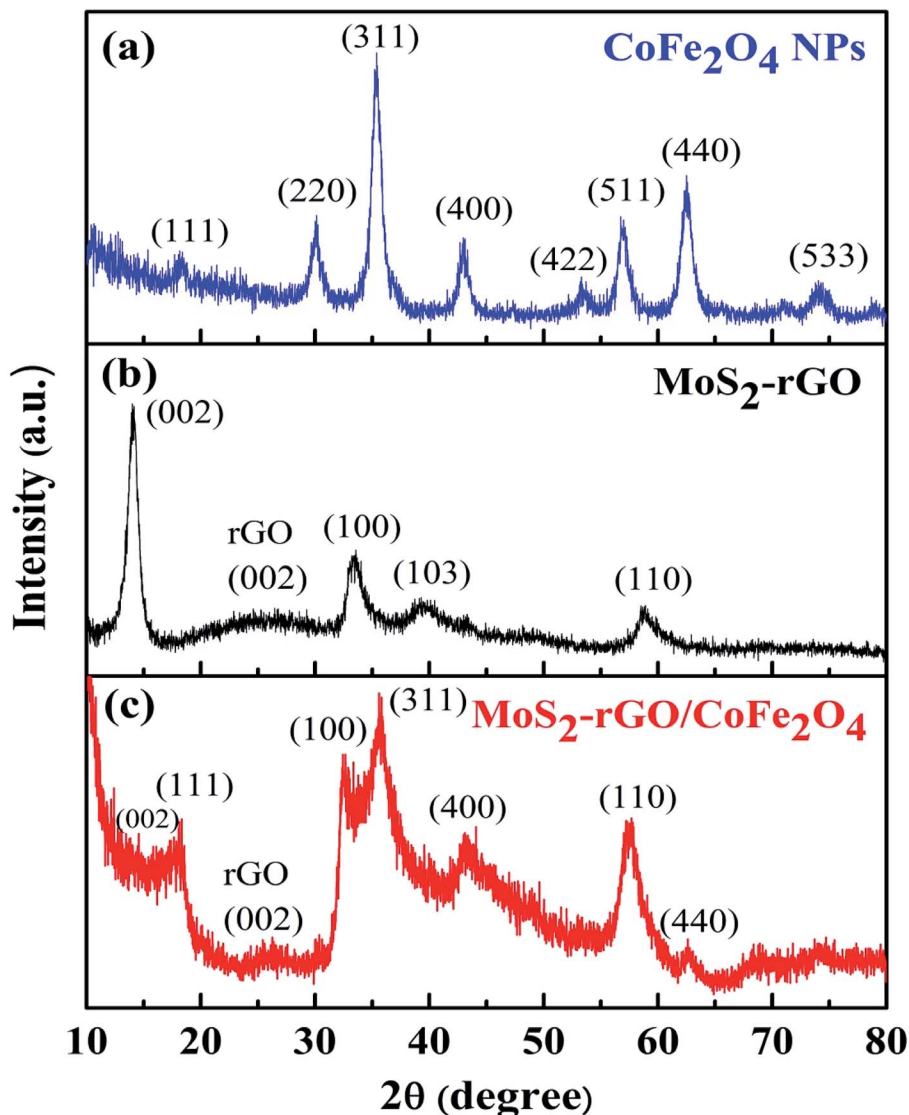
Fig. 2   XRD patterns of (a) $CoFe_2O_4$ nanoparticles, (b) MoS_2-rGO, and (c) the MoS_2-rGO/$CoFe_2O_4$ nanocomposite.

MoS_2-rGO/$CoFe_2O_4$ nanocomposite. The higher I_D/I_G values indicate that introducing $CoFe_2O_4$ nanoparticles creates a higher disorder degree and abundant defects edge structure in rGO to increase graphitization of C atoms during the preparation of the 3D hierarchical MoS_2-rGO/$CoFe_2O_4$ nanocomposite.[42]

3.2   Morphology analysis and elemental composition

The surface morphologies of MoS_2-rGO and MoS_2-rGO/$CoFe_2O_4$ nanocomposite were characterized using FESEM, and are shown in Fig. 4. From Fig. 4a and b, a uniform 3D flower-like MoS_2 microsphere was successfully prepared by self-assembly of a wrapped ultrathin layer MoS_2 nanosheet-like structure, and randomly distributed onto the entire surface of the rGO nanosheet with a diameter size of around 1–2 μm.[38,43] A flower-like MoS_2 microsphere consists of several interconnected massive nanopetals with serious agglomeration due to the high

concentration of molybdenum and sulfur vacancies.[28] Most of the surface of the rGO nanosheet was uniformly covered by an excellent loading of densely packed MoS_2 nanopetals.[44] In Fig. 4c and d, spherical $CoFe_2O_4$ nanoparticles and hierarchical flower-like MoS_2-rGO microspheres are mixed together consistently in the prepared MoS_2-rGO/$CoFe_2O_4$ nanocomposite. This does not destroy the 3D microsphere structure and shows numerous defect curled sites of the MoS_2 nanosheet on the surface of rGO nanosheet, as shown in Fig. 4c. From Fig. 4e, energy dispersive X-ray (EDX) analysis was used to illuminate the composition of the elements. The results confirmed the presence of Mo, S, C, O, Fe, and Co elements in the sample, with an atomic mass percent of 9.63, 29.90, 18.49, 29.41, 7.37 and 5.19%, respectively. The 3D hierarchical microsphere structure can expand the higher specific surface area to enhance interfacial polarization and defect dipole polarization, which is beneficial for greater attenuation of incident EM energy within the shield.
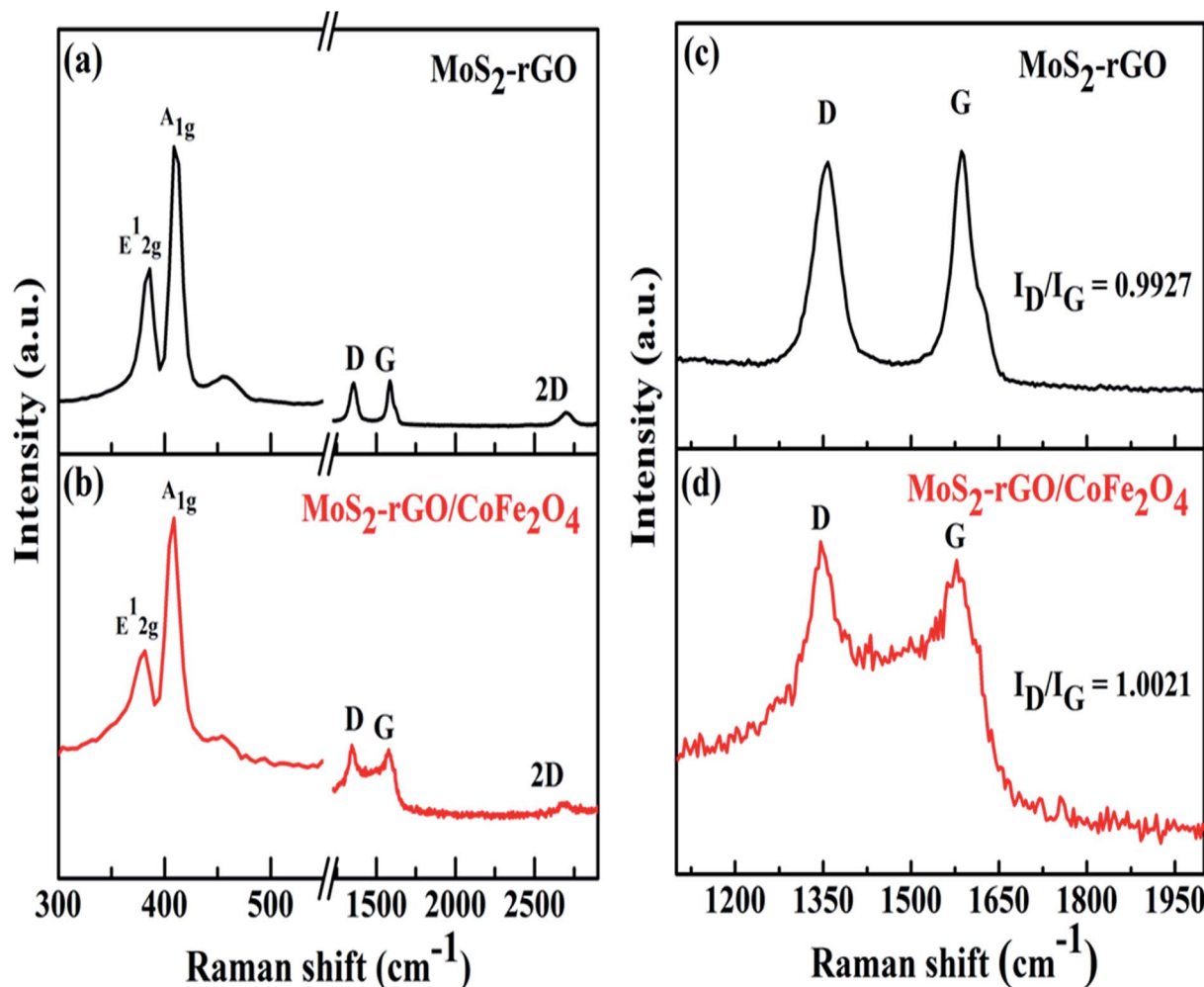
Fig. 3 Raman spectra of (a) MoS_2-rGO, and (b) the MoS_2-rGO/$CoFe_2O_4$ nanocomposite, and (c) and (d) enlarged views of the D and G bands.

HRTEM has been used to examine the microscopic structure of MoS_2-rGO and the MoS_2-rGO/$CoFe_2O_4$ nanocomposite, as depicted in Fig. 5. The dark contrast object MoS_2 is a fabricated wrapped nanosheet-like microstructure with plenty of folded edges well dispersed with a gray background rGO wrinkled paper-like morphology to form very close contact with each other, as shown in Fig. 5a.[38] The HRTEM image in Fig. 5b indicates that the interplanar distance of the fringes were estimated at around ∼0.62 nm at the edge of the crumpled paper-like structure and indexed to the (002) crystal plane of the layered crystalline MoS_2 with a hexagonal structure. MoS_2 uniformly dispersed on the surface of rGO nanosheet with d-spacing 0.34 nm corresponds to the (002) crystal plane of the rGO nanosheet.[28,29] Three diffraction rings well indexed to the (002), (100), and (110) reflections of MoS_2 and the (002) plane of rGO nanosheet were observed on the selected area electron diffraction (SAED) pattern (Fig. 5a). The HRTEM image in Fig. 5c shows that the spherical $CoFe_2O_4$ nanoparticles were randomly decorated on the surface of the MoS_2-rGO nanocomposite with an average diameter size of around 8–12 nm. From Fig. 5d, the lattice fringe with a d-spacing of spherical $CoFe_2O_4$ nanoparticles of 0.48 nm, corresponding to the (111) lattice plane, is consistent with the XRD results.

3.3 EMI shield performance of the nanocomposite

Scattering-parameters were carried-out with the help of a Vector Network Analyzer to investigate the incident microwave attenuation performance of the materials. The total shielding effectiveness (SE_T) of a material can be considered in the following terms; when an incident EM waves pass through a shield material, some is part absorbed (SE_A), some is reflected (SE_R), and the rest is transmitted or undergoes multiple reflections (SE_M) through the shield material. Therefore, SE_T is a function of the logarithmic ratio of incoming power (P_I) to outgoing power (P_T) of the EM wave, and represented in decibels (dBs) as follows:[5]

$$SE_T(dB) = -10 \log\left(\frac{P_T}{P_I}\right) = SE_R(dB) + SE_A(dB) + SE_M(dB)$$

(1)

The multiple reflection term (SE_M) value of the shielding material can be neglected when $SE_A \geq 10$ dB. Therefore, the total SE can be written as:[17]

$$SE_T (dB) = SE_R (dB) + SE_A (dB)$$

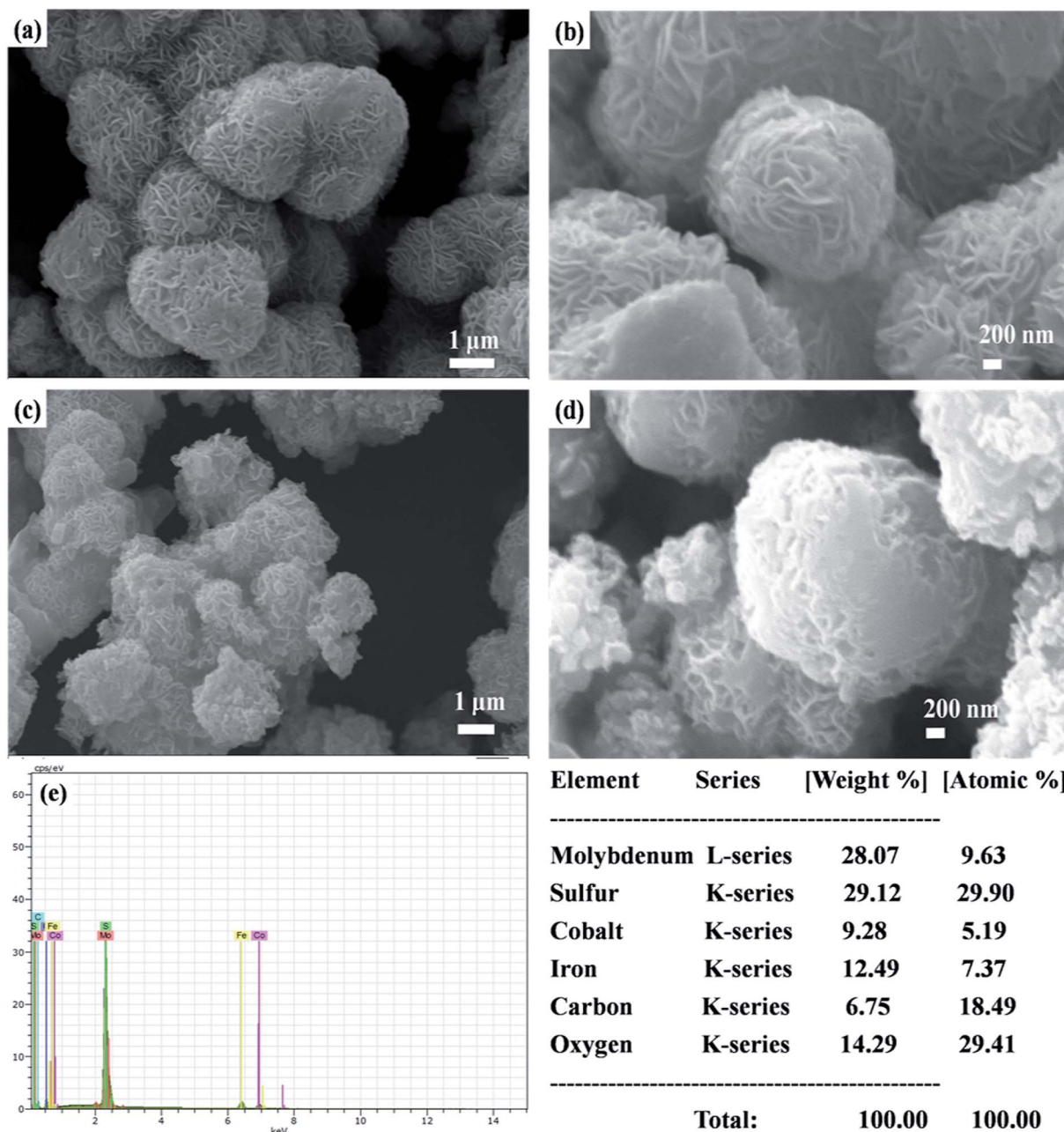| Element	Series	[Weight %]	[Atomic %]
Molybdenum	L-series	28.07	9.63
Sulfur	K-series	29.12	29.90
Cobalt	K-series	9.28	5.19
Iron	K-series	12.49	7.37
Carbon	K-series	6.75	18.49
Oxygen	K-series	14.29	29.41
Total:		100.00	100.00

Fig. 4 Typical SEM pictures of as-prepared (a) MoS_2-rGO and (c) the MoS_2-rGO/$CoFe_2O_4$ nanocomposite at low-magnification, and (b) MoS_2-rGO and (d) MoS_2-rGO/$CoFe_2O_4$ at high magnification. (e) EDX data from the MoS_2-rGO/$CoFe_2O_4$ nanocomposite.

Further, the SE_A and SE_R can be obtained regarding electrical conductivity (σ_{ac}), thickness of the shield (t), relative permeability (μ_r), and skin depth of the material (δ), expressed as:[28]

$$SE_R(dB) = 10 \log\left\{\frac{\sigma_{ac}}{16\omega\varepsilon_0\mu_r}\right\} \quad (2)$$

and

$$SE_A(dB) = 20\left\{\frac{t}{\delta}\right\}\log e = 20t\sqrt{\frac{(\omega\mu_r\sigma_{ac})}{2}} = 8.68\left\{\frac{t}{\delta}\right\} \quad (3)$$

The SE due to reflection decreases with increasing frequency and SE due to absorption increases with increasing frequency. A material exhibits higher reflection loss (SE_R) if it has larger electrical conductivity and smaller magnetic permeability; while a higher SE_A value is mainly attributed to both higher electrical conductivity and magnetic permeability of a material. The electrical conductivity (σ_{ac}) of a material is related to dielectric loss $\sigma_{ac} = \omega\varepsilon_0\varepsilon''$ and skin depth (δ) as $\delta = \frac{\sqrt{2}}{\sqrt{\sigma\omega\mu'}}$, respectively. The skin depth (δ) of a material decreases with increasing frequency (f), conductivity (σ), and permeability (μ).[8]
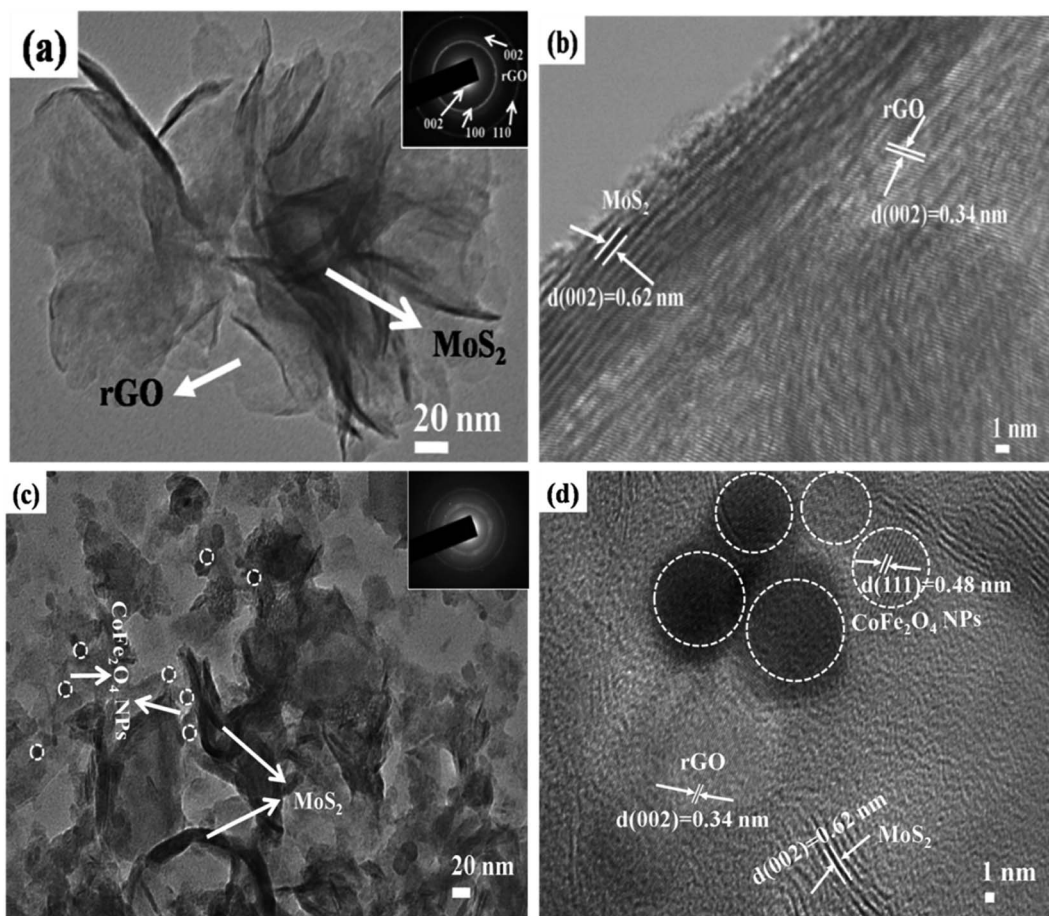
Fig. 5 TEM images of (a) MoS_2-rGO and (c) MoS_2-rGO/$CoFe_2O_4$ at low-resolution and (b) MoS_2-rGO and (d) MoS_2-rGO/$CoFe_2O_4$ at high-resolution.

For better understanding of the EMI shielding mechanism, various shielding parameters (SE_R, SE_A, and SE_T) were further analyzed in the desired frequency range (X-band), and are shown in Fig. 6. SE due to reflection (SE_R) is shown in Fig. 6a for the samples MoS_2, rGO, $CoFe_2O_4$, MoS_2-rGO, and the MoS_2-rGO/$CoFe_2O_4$ nanocomposite, and their values were found to be 2.71, 4.17, 1.52, 6.57, and 7.80 dB, respectively. On the other hand, Fig. 6b represents SE due to absorption (SE_A) for the same samples, with values 3.61, 9.69, 3.97, 10.60 and 12.62 dB, respectively. These graphs show that the contribution from
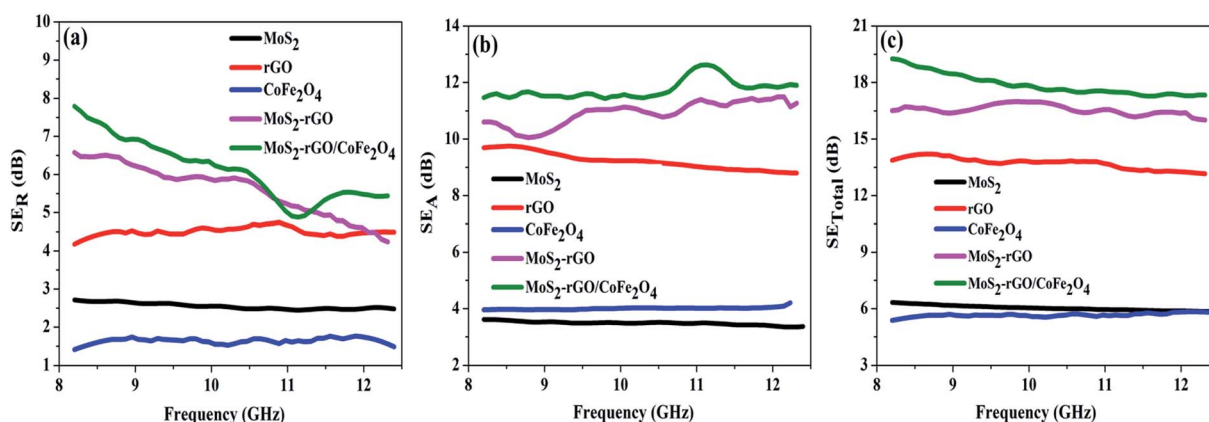

Fig. 6 Frequency dependence of the EMI shielding performance: (a) SE_R, (b) SE_A, and (c) SE_T values of MoS_2, rGO, $CoFe_2O_4$, MoS_2-rGO, and the MoS_2-rGO/$CoFe_2O_4$ nanocomposite in the X-band range.
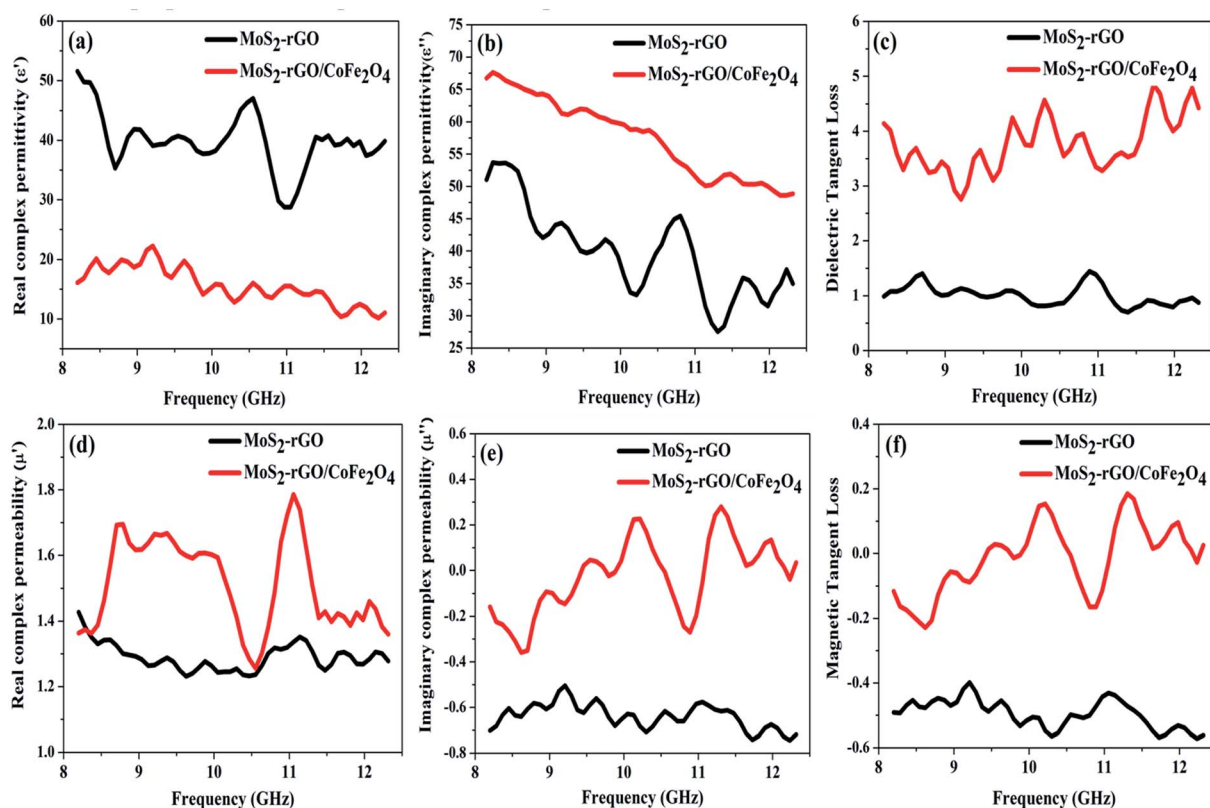
Fig. 7 Frequency dependence of the (a) and (b) complex permittivity, (d) and (e) complex permeability, and corresponding (c) dielectric loss tangent and (f) magnetic loss tangent of MoS_2-rGO and the MoS_2-rGO/$CoFe_2O_4$ nanocomposite.

reflection is much lower than the absorption, suggesting that absorption is the main mechanism for shielding effectiveness. The poor SE_R value is generally due to microwave impedance mismatching and is proportional to $\dfrac{\sigma_{ac}}{w\mu_r}$.[17] A material represents higher reflection loss (SE_R) if it has larger electrical conductivity and smaller magnetic content. The higher SE_A value attributed mainly to both higher electrical conductivity and magnetic permeability is directly proportional to $\sqrt{\sigma\mu}$.[27] These two parameters can be successfully enhanced by introducing rGO and $CoFe_2O_4$ nanoparticles in the MoS_2 nanosheet, and have a great influence on the EMI shielding effectiveness. The significantly improved EMI SE may contribute to the conductivity as rGO and magnetic content as $CoFe_2O_4$ nanoparticles, and serve as an excellent conductive and magnetic network in the MoS_2-rGO/$CoFe_2O_4$ nanocomposite. Therefore, a moderate value of electrical conductivity and impedance matching is required for materials with less SE due to reflection and more SE due to absorption. A superior MA and shielding performance is strongly dependent on defect dipole polarization, interfacial polarization, eddy current loss, and magnetic hysteresis loss, which ascribed most of the EM energy attenuated inside the shield. It is clear from Fig. 6c that the MoS_2 nanosheet shows the least value of SE_T (6.33 dB) due to the lack of magnetic content, whereas the $CoFe_2O_4$ nanoparticles show a similar poor performance SE_T (5.37 dB) because of low conductivity. The rGO nanosheet represents a higher SE_T

~13.87 dB due to higher electrical conductivity. A maximum value of total SE (SE_T) ~19.26 dB was achieved by the MoS_2-rGO/$CoFe_2O_4$ nanocomposite, suggesting more incident EM energy is absorbed inside the sample. This value is higher as compared with SE_T ~16.52 dB for MoS_2-rGO nanocomposite, indicating transparency to incoming EM energy, as shown in Fig. 6c. The total SE value of the MoS_2-rGO/$CoFe_2O_4$ nanocomposite continuously decreases with increasing frequency and suggests that the $CoFe_2O_4$ nanoparticles decorating the MoS_2-rGO nanocomposite exhibit excellent efficiency at a low-frequency range for EMI shielding performance, as displayed in Fig. 6c.

3.4 EM wave absorption performance of the nanocomposite

EM wave absorption performance of materials related to the relative complex permittivity (ε_r) were calculated using the Debye dipolar relaxation process and expressed as:[19]

$$\varepsilon_r = \varepsilon_\infty + \frac{(\varepsilon_s - \varepsilon_\infty)}{1 + j\omega\tau} = \varepsilon' - j\varepsilon''$$

$$\varepsilon' = \varepsilon_\infty \frac{(\varepsilon_s - \varepsilon_\infty)}{(1 + \omega^2\tau^2)} \tag{4}$$

and

$$\varepsilon'' = \frac{(\varepsilon_s - \varepsilon_\infty)\omega\tau}{(1 + \omega^2\tau^2)} + \frac{\sigma}{\omega\varepsilon_0} \tag{5}$$
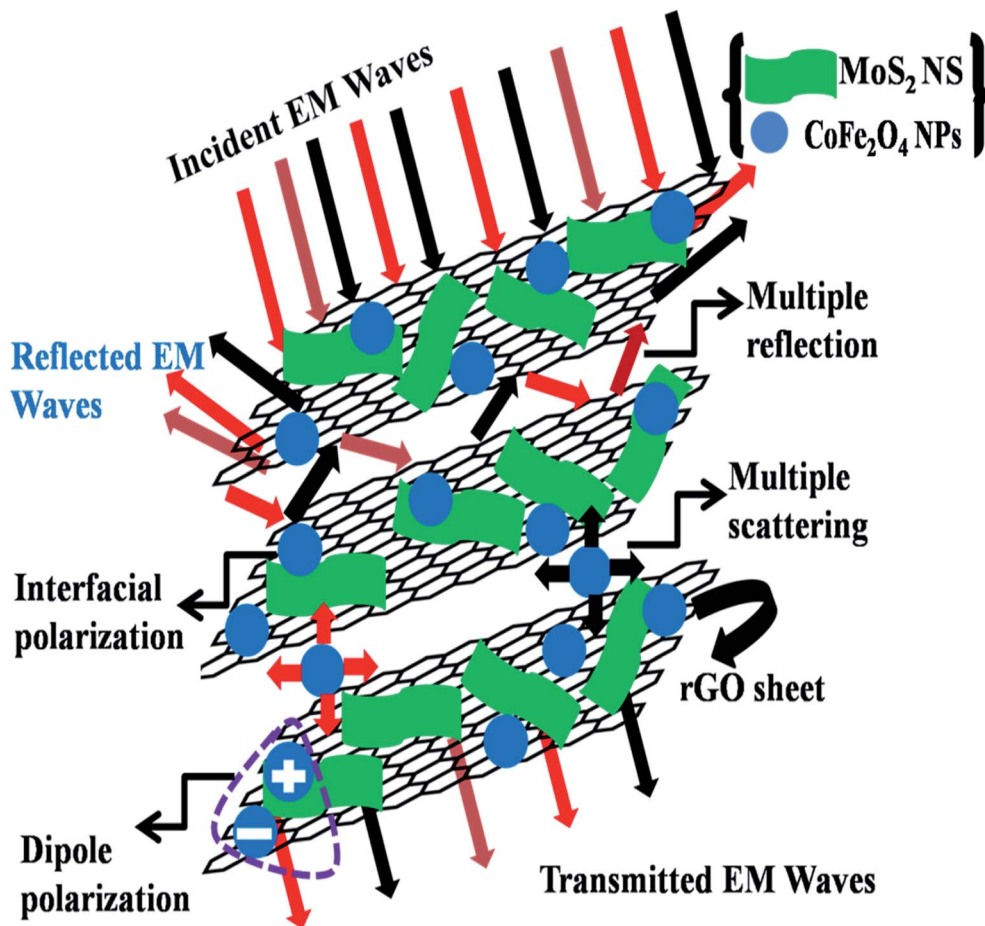
Fig. 8 A schematic illustration of the EMI shielding mechanism in the MoS_2-rGO/$CoFe_2O_4$ nanocomposite.

where, ω, ε_∞ and ε_s represent angular frequency, relative dielectric permittivity, and static permittivity at high-frequency limits, respectively. σ is electrical conductivity and ε_o is the dielectric constant in a vacuum ($\varepsilon_o = 8.85 \times 10^{-12}$ F m^{-1}), respectively. To better understand the MA mechanism, the frequency dependence of the real and imaginary part of the relative complex permittivity ($\varepsilon_r = \varepsilon' - j\varepsilon''$), and permeability ($\mu_r = \mu' - j\mu''$) of the nanocomposite are investigated, and the results are depicted in Fig. 7. Vector network analyzer tools were

used to measure the EM wave absorption performance in the frequency range of 8–12 GHz. The real value of complex permittivity (ε') and permeability (μ') represents the ability of a material to store incident EM energy through wave propagation, and the imaginary value of complex permittivity (ε'') and permeability (μ'') expressed as the ability of a material to attenuate more EM energy within the medium.[13,14] In Fig. 7a and b, the real (ε') and imaginary permittivity (ε'') decrease with increased frequency in the tested region. A material that has too

Table 1 Comparison of SE_{Total} values of the MoS_2-rGO/$CoFe_2O_4$ nanocomposites *vs.* other useful EMI shielding materials

Sr. No.	Sample name	Thickness (mm)	SE_{Total} (dB)	References
1	MoS_2-rGO/Fe_3O_4	1.3	8.27	Prasad *et al.*[28]
2	Graphene/PMMA (1.8 vol%)	2.4	16	Zhang *et al.*[45]
3	$La_{0.7}Sr_{0.3}MnO_3$ (100 wt%)	2	19	Reshi *et al.*[46]
4	Carbonyl iron/PVDF (50 wt%)	1.2	20	Joseph *et al.*[47]
5	rGO@Fe_3O_4/poly(etherimide)	2.5	14–18	Shen *et al.*[48]
6	rGO/Ba-ferrite	1	18	Verma *et al.*[49]
7	20% Gd@MoS_2-rGO	1.1	20.47	Prasad *et al.*[50]
8	MoS_2-rGO/$CoFe_2O_4$	1.4	19.26	Present work

high permittivity or permeability represents poor EM wave absorption performance, and suggests that relative permittivity and permeability are out of balance. An ideal EM wave absorption material possesses good impedance matching characteristics $\left(Z_r = Z_{in}/Z_0 = \sqrt{\mu_r/\varepsilon_r}\right)$ and indicates that the moderate of the permittivity and permeability ($\varepsilon_r \approx \mu_r$) should be close to $Z_r = 1$. This shows that all incident EM waves can enter inside shield materials.[15] In the MoS$_2$-rGO/CoFe$_2$O$_4$ nanocomposite, the imaginary permittivity (ε'') and dielectric loss $\left(\tan \delta_\varepsilon = \dfrac{\varepsilon''}{\varepsilon'}\right)$ was too high, at 67.62 and 4.84 as compared with 53.70, 1.44 for MoS$_2$-rGO nanocomposite, which indicates that more attenuation of EM energy can be achieved within the shield compared with pure MoS$_2$-rGO. In other words, the introduction of magnetic nanoparticles plays an important role in higher ε'' values due to the formation of a highly conductive and magnetic filler with a large surface area, leading to migration of charges at multi-interfaces between MoS$_2$, rGO, and CoFe$_2$O$_4$ and generating interfacial polarization. The complex permeability μ' and μ'' values of MoS$_2$-rGO/CoFe$_2$O$_4$ nanocomposite are slightly higher than MoS$_2$-rGO. Reasons that the introduction of CoFe$_2$O$_4$ nanoparticles represents a little sign of a magnetic ascension leading to enhanced complex permeability of materials and the results are presented in Fig. 7d and e. On other hand, low μ' and μ'' values of the MoS$_2$-rGO nanocomposite, leads to degradation of the impedance matching performance and originates from the poor magnetic property of the materials.

We have also calculated dielectric loss tangent $\left(\tan \delta_\varepsilon = \dfrac{\varepsilon''}{\varepsilon'}\right)$ and magnetic loss tangent $\left(\tan \delta_\mu = \dfrac{\mu''}{\mu'}\right)$ of as-prepared nanocomposite with the help of relative complex permittivity (ε_r), permeability (μ_r), and used this to appreciate dissipation capacity of the incident EM energy within the medium, as shown in Fig. 7c and f.[28] The dielectric loss ability of the material is due to multiple interfacial polarization, defect dipole polarization, conductance loss, and space charge polarization, while magnetic loss ability is mainly associated with natural resonance loss, anisotropy energy loss, eddy current loss, and magnetic hysteresis loss, respectively.[24] Ideal MA materials should exhibit higher dielectric loss and magnetic loss, and their ratio should be around ∼1 for proper impedance matching for strong attenuation of EM energy inside the shield sample.[13] In Fig. 7c and f, the value of $\tan \delta_\mu$ is much lower than the value of $\tan \delta_\varepsilon$, suggesting that the magnetic content in the nanocomposite is very low. Thus, this result indicates that the EM wave attenuation mechanism for MA performance is mainly associated with the dielectric loss instead of the magnetic loss. The μ'' and magnetic loss value for MoS$_2$-rGO and MoS$_2$-rGO/CoFe$_2$O$_4$ nanocomposite are negative in Fig. 7e and f, which suggests that magnetic energy is emitted away from these

materials owing to the migration of charge carriers. Further, the existence of a higher disorder degree and abundant defects/functional groups, specific surface area, multiple reflections and scattering inside the shield play an essential role in enhancing the microwave shielding effectiveness of the MoS$_2$-rGO/CoFe$_2$O$_4$ nanocomposite. From these observed outcomes, this may be making a final decision that MoS$_2$-rGO/CoFe$_2$O$_4$ nanocomposite has excellent dissipation ability of the incident EM waves compared with the pure MoS$_2$-rGO nanocomposite.

There are several reasons behind the synthesized MoS$_2$-rGO/CoFe$_2$O$_4$ nanocomposite having an excellent MA and EMI shielding performance. The MoS$_2$ nanosheet shows excellent dielectric loss of materials and possesses multiple interface structures and dipole polarization charges on the surface of the nanosheet to enhance interface polarization and defect dipole polarization. The rGO nanosheet represents highly conductive materials with a strong dielectric loss due to abundant defects on its surface and many functional groups with high specific surface area. CoFe$_2$O$_4$ nanoparticles are magnetic loss absorbent, and the introduction can improve the impedance matching properties of the MoS$_2$-rGO/CoFe$_2$O$_4$ nanocomposite. The enhanced dielectric loss and magnetic loss allow a novel route for the development of MA performance and excellent shielding effectiveness due to absorption. A pictorial model of the superb microwave shielding phenomenon is demonstrated in Fig. 8.

A detailed comparison of SE$_{Total}$ of MoS$_2$-rGO/CoFe$_2$O$_4$ nanocomposite and some useful EMI shielding materials are listed in Table 1.

4. Conclusions

In summary, CoFe$_2$O$_4$ nanoparticles decorated onto the surface of a MoS$_2$-rGO nanocomposite have been successfully synthesized by a simple two-step hydrothermal method. HRTEM results confirmed the decoration of CoFe$_2$O$_4$ nanoparticles onto the surface of the MoS$_2$-rGO nanocomposite with a size of around 8–12 nm. CoFe$_2$O$_4$ nanoparticles can act as a highly conductive and magnetic filler with a large surface area and favor proper impedance matching to improve dielectric loss and magnetic loss of the materials. Total SE (SE$_T$ ∼19.26 dB) was achieved for the MoS$_2$-rGO/CoFe$_2$O$_4$ nanocomposite, suggesting more incident EM energy was absorbed, while the pure MoS$_2$-rGO nanocomposite presents total SE (SE$_T$ ∼16.52 dB) and indicates transparency to incoming EM energy. The multiple interfacial polarizations, defect dipole polarization and eddy current loss contribute to the strong attenuation loss ability of incident EM energy within the shield materials. Thus, this work suggests that the MoS$_2$-rGO/CoFe$_2$O$_4$ nanocomposite is a potential candidate and can be widely applied to EM pollution cleaning, wireless telecommunications, military weapons, and human health care.

Conflicts of interest

There are no conflicts to declare.

Acknowledgements

References

1 K. Zhang, X. Gao, Q. Zhang, T. Li, H. Chen and X. Chen, *J. Alloys Compd.*, 2017, **721**, 268–275.

2 J. Zhang, R. Shu, C. Guo, R. Sun, Y. Chen and J. Yuan, *J. Alloys Compd.*, 2019, **784**, 422–430.

3 F. Shahzad, P. Kumar, S. Yu, S. Lee, Y. H. Kim, S. M. Hong and C. M. Koo, *J. Mater. Chem. C*, 2015, **3**, 9802–9810.

4 R. Kumar, H. K. Choudhary, S. P. Pawar, S. Bose and B. Sahoo, *Phys. Chem. Chem. Phys.*, 2017, **19**, 23268–23279.

5 S. Singh, P. Tripathi, A. Bhatnagar, Ch. R. P. Patel, A. P. Singh, S. K. Dhawan, B. P. Gupta and O. N. Srivastava, *RSC Adv.*, 2015, **5**, 107083–107087.

6 S. Umrao, T. K. Gupta, S. Kumar, V. K. Singh, M. K. Sultania, J. H. Jung, I. K. Oh and A. Srivastava, *ACS Appl. Mater. Interfaces*, 2015, **7**, 19831–19842.

7 A. P. Guo, X. J. Zhang, S. W. Wang, J. Q. Zhu, L. Yang and G. S. Wang, *ChemPlusChem*, 2016, **81**, 1305–1311.

8 A. P. Guo, X. J. Zhang, J. K. Qu, S. W. Wang, J. Q. Zhu, G. S. Wang and L. Guo, *Mater. Chem. Front.*, 2017, **1**, 2519–2526.

9 Y. Zhou, Q. Wen, Z. Ren, H. Xie, S. Tao and W. Zhou, *J. Alloys Compd.*, 2018, **733**, 33–39.

10 W. Zhang, X. Zhang, H. Wu, H. Yan and S. Qi, *J. Alloys Compd.*, 2018, **751**, 34–42.

11 J. Wang, X. Lin, R. Zhang, Z. Chu and Z. Huang, *J. Alloys Compd.*, 2018, **743**, 26–35.

12 Q. L. Wen, W. C. Zhou, J. B. Su, Y. C. Qing, F. Luo and D. M. Zhu, *J. Alloys Compd.*, 2016, **666**, 359–365.

13 M. Li, X. Cao, S. Zheng and S. Qi, *J. Mater. Sci.: Mater. Electron.*, 2017, **28**, 16802–16812.

14 E. Yang, X. Qi, R. Xie, Z. Bai, Y. Jiang, S. Qin, W. Zhong and Y. Du, *Appl. Surf. Sci.*, 2018, **442**, 622–629.

15 B. Quan, X. Liang, G. Xu, Y. Cheng, Y. Zhang, W. Liu, G. Ji and Y. Du, *New J. Chem.*, 2017, **41**, 1259–1266.

16 B. P. Singh, D. K. Saket, A. P. Singh, S. Pati, T. K. Gupta, V. N. Singh, S. R. Dhakate, S. K. Dhawan, R. K. Kotnala and R. B. Mathur, *J. Mater. Chem. A*, 2015, **3**, 13203–13209.

17 A. P. Singh, P. Garg, F. Alam, K. Singh, R. B. Mathur, R. P. Tandon, A. Chandra and S. K. Dhawan, *Carbon*, 2012, **50**, 3868–3875.

18 X. Liang, X. Zhang, W. Liu, D. Tang, B. Zhang and G. Ji, *J. Mater. Chem. C*, 2016, **4**, 6816–6821.

19 A. Xie, M. Sun, K. Zhang, W. Jiang, F. Wu and M. He, *Phys. Chem. Chem. Phys.*, 2016, **18**, 24931–24936.

20 B. Zhao, W. Zhao, G. Shao, B. Fan and R. Zhang, *ACS Appl. Mater. Interfaces*, 2015, **7**, 12951–12960.

21 X. Sun, J. He, G. Li, J. Tang, T. Wang, Y. Guo and H. Xue, *J. Mater. Chem. C*, 2013, **1**, 765–777.

22 J. Zhang, R. Shu, Y. Ma, X. Tang and G. Zhang, *J. Alloys Compd.*, 2019, **777**, 1115–1123.

23 M. Q. Ning, M. M. Lu, J. B. Li, Z. Chen, Y. K. Dou, C. Z. Wang, F. Rehman, M. S. Cao and H. B. Jin, *Nanoscale*, 2015, **7**, 15734–15740.

24 M. Cao, C. Han, X. Wang, M. Zhang, Y. Zhang, J. Shu, H. Yang, X. Fang and J. Yuan, *J. Mater. Chem. C*, 2018, **6**, 4586–4602.

25 X. Ding, Y. Huang, S. Li, N. Zhang and J. Wang, *Composites, Part A*, 2016, **90**, 424–432.

26 Y. Sun, W. Zhong, Y. Wang, X. Xu, T. Wang, L. Wu and Y. Du, *ACS Appl. Mater. Interfaces*, 2017, **9**, 34243–34255.

27 Y. Yang, M. Li, Y. Wu, T. Wang, E. S. Choo, J. Ding, B. Zong, Z. Yang and J. Xue, *Nanoscale*, 2016, **8**, 15989–15998.

28 J. Prasad, A. K. Singh, J. Shah, R. K. Kotnala and K. Singh, *Mater. Res. Express*, 2018, **5**, 055028–055038.

29 X. Wang, W. Zhang, X. Ji, B. Zhang, M. Yu, W. Zhang and J. Liu, *RSC Adv.*, 2016, **6**, 106187–106193.

30 D. Zhang, Y. Jia, J. Cheng, S. Chen, J. Chai, X. Yang, Z. Wu, H. Wang, W. Zhang, Z. Zhao, C. Han, M. Cao and G. P. Zheng, *J. Alloys Compd.*, 2018, **758**, 62–71.

31 M. Sabet, H. Jahangiri and E. Ghashghaei, *J. Mater. Sci.: Mater. Electron.*, 2018, **29**, 10853–10863.

32 L. Staudenmaier, Verfahren zur darstellung der graphitsäure, *Ber. Dtsch. Chem. Ges.*, 1898, **31**, 1481–1487.

33 V. Georgiadou, C. Kokotidou, B. L. Droumaguet, B. Carbonnier, T. C. Papadopoulou and C. D. Samara, *Dalton Trans.*, 2014, **43**, 6377–6388.

34 G. Feng, A. Wei, Y. Zhao and J. Liu, *J. Mater. Sci.: Mater. Electron.*, 2015, **26**, 8160–8166.

35 W. Zhang, L. Li, W. Zhu, H. Yan and S. Qi, *J. Mater. Sci.: Mater. Electron.*, 2017, **28**, 15488–15494.

36 X. Su, D. Wang, Q. Yan, X. Guo, S. Fang and Y. Liu, *J. Mater. Sci.: Mater. Electron.*, 2018, **29**, 4020–4029.

37 J. Yang, M. Ye, A. Han, Y. Zhang and K. Zhang, *J. Mater. Sci.: Mater. Electron.*, 2019, **30**, 292–301.

38 L. Wu, X. Xu, Y. Zhao, K. Zhang, Y. Sun, T. Wang, Y. Wang, W. Zhong and Y. Du, *Appl. Surf. Sci.*, 2017, **425**, 470–477.

39 W. Xiao, W. Zhou, T. Feng, Y. Zhang, H. Liu and L. Tian, *Materials*, 2016, **9**, 783–796.

40 S. Ahmed, X. Ding, N. Bao, P. Bian, R. Zheng, Y. Wang, P. P. Murmu, J. V. Kennedy, R. Liu, H. Fan, K. Suzuki, J. Ding and J. Yi, *Chem. Mater.*, 2017, **29**, 9066–9074.

41 Y. Shang, T. Li, Y. Yin, H. Li, L. Zhang, J. Lyu, C. Xiong and T. Zhao, *Chem. Lett.*, 2017, **46**, 527–529.

42 A. Naskar, H. Khan and S. Jana, *J. Sol-Gel Sci. Technol.*, 2018, **86**, 599–609.

43 J. Xiang, D. Dong, F. Wen, J. Zhao, X. Zhang, L. Wang and Z. Liu, *J. Alloys Compd.*, 2016, **660**, 11–16.

44 N. A. Alarfaj, M. F. E. Tohamy and H. Oraby, *New J. Chem.*, 2018, **42**, 11046–11053.

45 H. B. Zhang, Q. Yan, W. G. Zheng, Z. He and Z. Z. Yu, *ACS Appl. Mater. Interfaces*, 2011, **3**, 918–924.

46 H. A. Reshi, A. P. Singh, S. Pillai, R. S. Yadav, S. K. Dhawan and V. Shelke, *J. Mater. Chem. C*, 2015, **3**, 820–827.

47 N. Joseph and M. T. Sebastian, *Mater. Lett.*, 2013, **90**, 64–67.

48 B. Shen, W. Zhai, M. Tao, J. Ling and W. Zheng, *ACS Appl. Mater. Interfaces*, 2013, **5**, 11383–11391.

49 M. Verma, A. P. Singh, P. Sambyal, B. P. Singh, S. K. Dhawan and V. Choudhary, *Phys. Chem. Chem. Phys.*, 2015, **17**, 1610–1618.

50 J. Prasad, A. K. Singh, K. K. Haldar, V. Gupta and K. Singh, *J. Alloys Compd.*, 2019, **788**, 861–872.